Available online at www.sciencedirect.com
ScienceDirect
Thin Solid Films 516 (2008) 5217–5222
www.elsevier.com/locate/tsf

Structural and Optical Studies on Ion-implanted 6H–SiC Thin Films

Z.C. Feng [a,*], S.C. Lien [a], J.H. Zhao [b], X.W. Sun [c], W. Lu [d]

[a] Graduate Institute of Electro-Optical Engineering, and Department of Electrical Engineering, National Taiwan University, Taipei, 106-17, Taiwan, ROC
[b] Department of Electrical and Computer Engineering, Rutgers University, Piscataway, NJ 08855, USA
[c] Nanyang Technological University, School of Electrical and Electronic Engineering, Singapore 639798, Singapore
[d] Department of Chemistry, Fisk University, Nashville, TN 37208, USA

Available online 14 July 2007

Abstract

A series of hot (600 °C) and room temperature C^+/Al^+ co-implanted 6H–SiC epitaxial films, under different implantation dose levels and high temperature (1550 °C) post-annealing, were studied by a variety of structural and optical characterization techniques, including secondary ion mass spectroscopy, high resolution X-ray diffraction, Fourier transform infrared reflectance, micro-Raman and photoluminescence (PL) spectroscopy. The damage and amorphization of SiC layer by co-implantation, and the elimination/suppression of the implantation induced amorphous layer via high temperature annealing are observed. The recovery of the crystallinity and the activation of the implant acceptors are confirmed. The results from hot or RT co-implantation are compared.

Keywords: 6H–SiC; Ion implantation; Annealing; Structure; Optics; Characterization

1. Introduction

Silicon carbide (SiC) and its polytypes are promising semiconductors for high temperature, high frequency, high radiation tolerance, high power electronic and optoelectronic applications, due to their extraordinary material properties such as large bandgap, high electron saturation velocity, high breakdown field and high thermal conductivity [1–3]. A great deal of research and development (R&D) interests and various device applications using 6H-, 4H- and other poly-types of SiC have emerged in recent years [1–5].

For SiC devices and processing developments, it is difficult to use the conventional diffusion techniques to produce the SiC-based p–n junctions and devices, because of the extremely high temperatures (~2000 °C) required for dopant diffusion [6,7]. Ion implantation appears as the primary technique for the SiC-based device development [7,8], and in particular, it is suitable for the selective doping in SiC device fabrication. The n-type doping with a high density of donor activation in SiC can be obtained by N ion implantation [8–10]. N^+ implantation into p-type 6H– and 4H–SiC epilayers at room and elevated temperatures has also been succeeded [11]. Efforts on the p-type Al and B ion-implantation into 6H–SiC have been made [12,13].

Although a number of efforts has been made on the p-type ion implantation in SiC, the acceptor activation in ion-implanted SiC remains an issue [6,12]. Ion implantation usually produces severe damage of the crystalline structure, and post-implantation annealing at temperatures higher than 1500 °C are necessary to recover the crystallinity and to electrically active the implanted ions [8,10].

To find a good way to improve the acceptor implant activation in SiC, we have explored the C–Al co-implantation [14–16]. The Al is a preferred acceptor in SiC due to its lower activation energy (0.24 eV) than other acceptors (0.33 eV for Ga and 0.33–0.7 eV for B) [8]. Carbon co-implantation is assumed to produce more Si vacancies and to improve Al acceptor activation [14], although adverse effects have been reported [12]. Electrical characterization has shown a large reduction of both the sheet resistivity in the C–Al co-implanted 6H–SiC epilayer and the specific contact resistivity of Al contacts made on C–Al implanted layer, indicating enhanced acceptor activation efficiency [14,15]. Preliminary optical measurements have also provided the evidence on the activation of acceptors and the recrystallization of C–Al co-implanted 6H–SiC by high

* Corresponding author. Tel.: +886 2 3366 3543; fax: +886 2 2367 7467.
E-mail address: zcfeng@cc.ee.ntu.edu.tw (Z.C. Feng).

0040-6090/$ - see front matter © 2007 Elsevier B.V. All rights reserved.
doi:10.1016/j.tsf.2007.07.094

Table 1
Ion implantation concentration and temperature

Type/concentration (cm^{-3})	Temperature and sample no.
C^+: 6×10^{20}, Al^+: 6×10^{20}	600 °C (E2) RT (E3)
C^+: 8×10^{20}, Al^+: 8×10^{20}	600 °C (E5) RT (E6)
C^+: 1×10^{21}, Al^+: 1×10^{21}	600 °C (F2) RT (F3)
C^+: 2×10^{21}, Al^+: 2×10^{21}	600 °C (F4) RT (F5)
Al^+: 2×10^{21}	600 °C (F6)

temperature annealing [16]. However, comprehensive studies on the C–Al co-implantation into SiC materials and related phenomena as well as physical mechanism are still needed.

In this work, we perform a penetrating study for the effects of Al–C ion co-implantation on epitaxial n^-/n^+ 6H–SiC and high temperature annealing. A series of n-type (doped with nitrogen to $\sim1\times10^{16}$ cm^{-3}) 6H–SiC epitaxial films ($\sim$10 μm thick) grown on n^+ ($\sim1\times10^{18}$ cm^{-3}) 6H–SiC substrates were used for Al^+–C^+co-implantation with different dose levels (6–20×10^{20} cm^{-3}) and at different temperatures ($\sim$25 °C and 600 °C). These implanted SiC materials were measured before and after annealing by way of a variety of structural and optical characterization techniques, including secondary ion mass spectroscopy (SIMS), high resolution X-ray diffraction (HRXRD), Fourier transform infrared (FTIR) reflectance, micro-Raman and photoluminescence (PL) spectroscopy. Various results and related interesting phenomena are discussed.

2. Experiment

Commercial n^-/n^+6H–SiC epitaxial wafers with 10-μm thick lightly N-doped ($\sim10\times10^{16}$ cm^{-3}) layers grown on highly N-doped ($\sim10\times10^{18}$ cm^{-3}), purchased from CREE, Inc., were used for ion-implantation in this study. Each wafer was implanted either first with C^+ then followed by Al^+ at either room temperature (RT) or 600 °C. Multiple implantations with various energies ranging from 20 to 120 keV for C^+ and from 50 to 200 keV for Al^+ as well as 500 Å thick Si_3N_4 coating were used to obtain a box-like implant profile near the surface with a thickness of 2000 Å with equal C^+ and Al^+ volume concentrations. Samples with several different Al concentrations ranging from 6×10^{20} to 2×10^{21} cm^{-3} were prepared to investigate concentration dependences. The post-implantation annealing was performed at 1550 °C for 30 min in a pure Ar gas ambient by using a conventional furnace. The implanted samples with the Si_3N_4 coating removed were placed in a graphite crucible in a face-to-face configuration during annealing.

A series of C^+–Al^+ co-implanted (with implant energies of 50–200 keV) 6H–SiC epitaxial films, ~10 μm thick, n-type doped with nitrogen to $\sim1\times10^{16}$ cm^{-3} and grown on n^+ ($\sim1\times10^{18}$ cm^{-3}) 6H–SiC substrates, were studied and listed in Table 1. There are four pairs of samples with each pair consisting of two samples with the same C^+–Al^+ implanted concentrations but under hot (600 °C) or room temperature (RT), and an Al^+ alone implanted one (F6). Each sample has a corner covered when doing ion implantation, which can be used for comparative measurements on un-implanted region.

All experimental samples were measured by structural and optical characterization techniques, including secondary ion mass spectroscopy (SIMS), high resolution X-ray diffraction (HR–XRD), Fourier transform infrared (FTIR) reflectance, micro-Raman and photoluminescence (PL) spectroscopy.

The SIMS depth profile measurements were performed in a VG SIMSLAB system which incorporates a quadru-pole mass spectrometer. Ar^+ ions from a duoplasatron ion gun were used as the primary beam, with the acceleration voltage set at 9 kV and beam current at 250 nA, which corresponds to a current density of 21.3 μA/cm^2.

High resolution X-ray diffraction (HRXRD) was measured using a Philips X'pert four crystal X-ray diffractometer. Two Renishaw Raman microscope systems with 514 nm and 325 nm excitations were used for Raman and photoluminescence (PL)

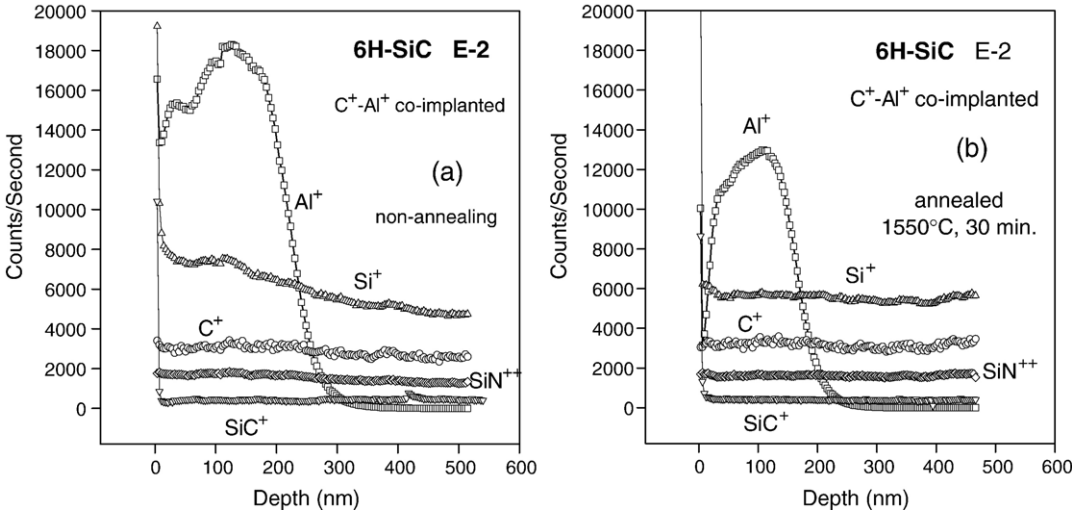

Fig. 1. SIMS depth profiles of an Al^+–C^+ co-implanted 6 H–SiC, E2 (C^+: 6×10^{20}, Al^+: 6×10^{20}, at 600 °C), (a) before annealing and (b) after annealing at 1550 °C, 30 min. The primary beam is at 9 kV and 250 nA, 10% gated flooding gun on.

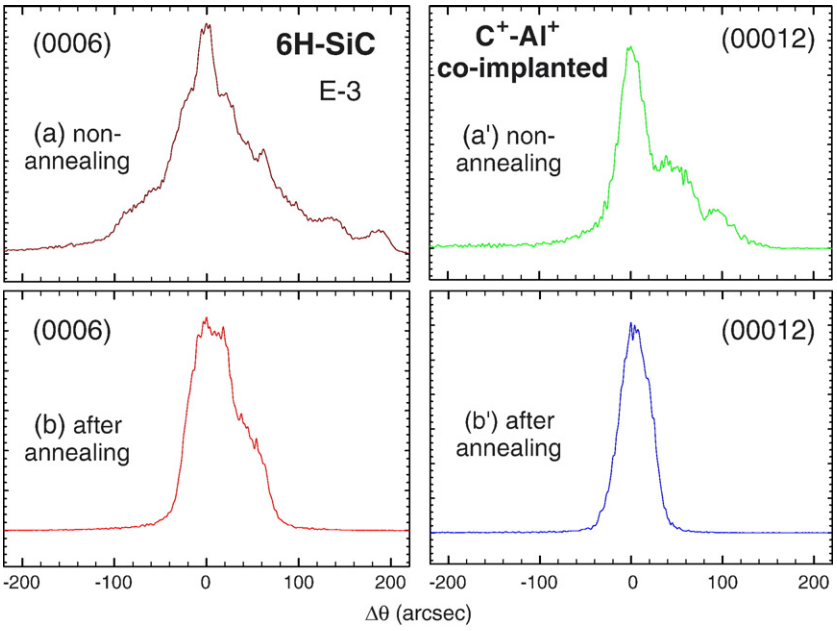

Fig. 2. HRXRD (0006) and (00012) patterns for a C^+–Al^+ co-implanted 6 H–SiC, E3 (C^+: 6×10^{20}, Al^+: 6×10^{20}, at RT), before and after annealing.

measurements at RT FTIR reflectance was measured by a Bio-Rad 175C FTIR spectrometer.

3. Results and discussion

3.1. Secondary ion mass spectroscopy (SIMS):

The SIMS depth profiles of the sample E2, implanted with both C^+ and Al^+ of 6×10^{20} cm^{-3} and at 600 °C, before and after annealing are presented in Fig. 1. The Al^+ depth profile of E2 before annealing shows a Gaussian distribution in a projected range of about 130 nm with a FWHM of about 150 nm. The Gaussian profile is skewed towards the surface as has been observed in numerous studies on silicon [17]. The Al^+ depth profile of E2 after annealing shows a shift of the Al^+peak towards the surface. The variation of the profile is due to the diffusion of Al dopant away from the maximum Al concentration, and is predicted from theory to be due to the inclusion of a diffusion term $D\tau$, where D is the diffusion coefficient and τ the

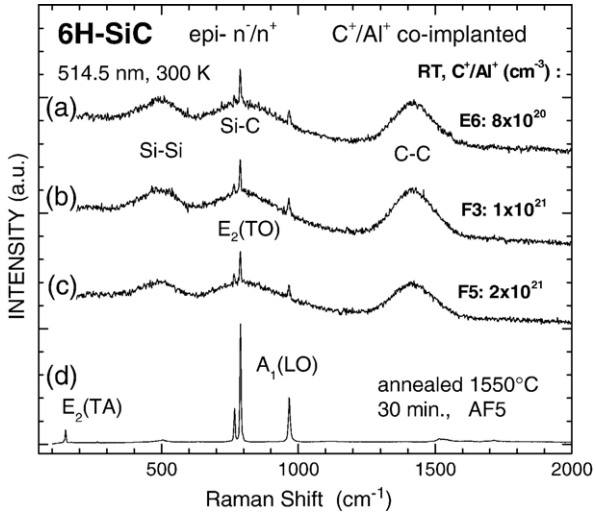

Fig. 3. Raman spectra, under 514 nm excitation, from three n^-/n^+ epitaxial 6 H–SiC with C–Al ions co- implanted at RT with different concentrations, (a)–(c), and an annealed sample, (d).

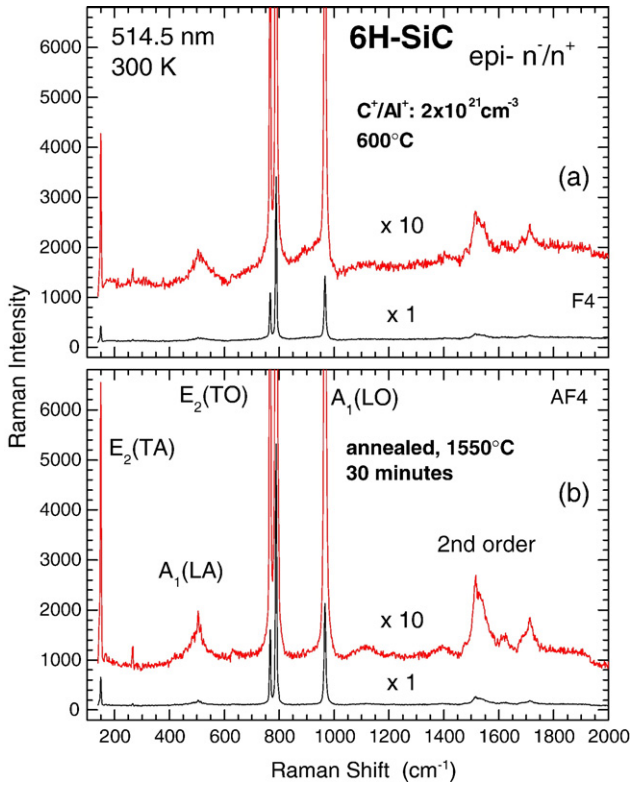

Fig. 4. Raman spectra, excited under 514 nm, from a hot (600 °C) C^+–Al^+ co-implanted 6 H–SiC, F4, with a concentration of 2×10^{21} cm^{-3} for C^+/Al^+, (a) before and (b) after annealing at 1550 °C for 30 minutes.

annealing time, into the standard deviation of the Gaussian profile [18]. From a comparison of Fig. 1(a) and (b), it is seen a decrease of the peak counts and the total amount of Al^+ dopants after annealing. Since most of the dopants diffusing towards the surface do not escape, this might be caused by the non-uniformity of the ion implantation on the experimental samples. But both resultant profiles are formed by adding two Gaussian functions symmetrical with respect to the plane of the sample surface which is equivalent to reflecting all out-diffusing atoms from the surface. This causes the Al dopant concentration near the surface to build up, leading to a resultant shift in the peak profile towards the surface. Diffusion of Al dopants towards the surface is further enhanced by ion-beam induced defects and dislocations creating low energy diffusion pathways.

3.2. High resolution X-ray diffraction (HRXRD)

The 6H–SiC characteristic (0006) and (00012) patterns of X-ray diffraction at 35.65 ° and 75.54 °, respectively, were examined for all the samples before and after annealing. Fig. 2 shows the high resolution XRD rocking curves of an Al–C co-implanted 6H–SiC sample E3, co-implanted at RT with both C^+ and Al^+ of 6×10^{20} cm^{-3}, before and after annealing. Right after the co-implantation without annealing, the (0006) and (00012) patterns exhibit more multiple diffraction features, indicating the box-structure of implanted ions. After annealing, these multiple diffraction features decreased greatly, predicting a smooth of the implanted ion profile distribution.

3.3. Raman scattering under visible 514.5 nm excitation

Fig. 3 shows micro-Raman spectra from three n^-/n^+ epitaxial 6H–SiC with co-implanted C–Al ions at RT with different concentrations of (a) E6, C^+ and Al^+ of 8×10^{20} cm^{-3}, (b) F3, C^+ and Al^+ of 1×10^{21} cm^{-3}, (c) F5, C^+ and Al^+ of 2×10^{21} cm^{-3}, and an annealed sample AF5 (annealed from F5 under 1500 °C for 30 min). The spectrum for the non-implanted corner exhibits the main Raman modes for a perfect 6H–SiC crystal [16]. After C^+–Al^+ co-implantation at RT with different concentrations, three broad Raman bands appeared, with the band center at near 500, 800 and 1420 cm^{-1}, respectively, as shown in Fig. 3(a)–(c). They are caused by Si–Si, Si–C and C–C vibrations, respectively, which are typical for amorphous SiC [19]. Single crystalline 6H–SiC characteristic Raman bands [20] of two E_2(TO) and one A_1(LO) are weakly superposed on the top of the Si–C amorphous band. These indicate the damage of 6H–SiC crystallinity and the formation of amorphous phase due to the ion implantation. However, after annealing at 1550 °C for 30 minutes, these broad features are almost eliminated, and a Raman spectrum similar to that from a single crystalline 6H–SiC appears as shown in Fig. 3(d), indicating the recovery of the SiC crystalline structure.

Samples under C^+–Al^+ hot implantation at 600 °C and before annealing showed quite different Raman spectral shapes. They did not show the three strong amorphous bands as shown in Fig. 3(a)–(c), instead, they showed only very weak amorphous features, as shown in Fig. 4 (a), with major features from crystalline 6H–SiC. This indicates that the hot implantation causes much less damage in 6H–SiC than that for RT ion co-implantation. After annealing at 1550 °C for 30 minutes, they exhibited μ-RS of Fig. 4(b), which is close to Fig. 3(d). Comparing two magnified (by a factor 10) spectra in Fig. 4(a)–(b), it can be found that after high temperature annealing, the weak a-SiC features have been further suppressed. The Raman spectrum from the hot-implanted/annealed sample is very close to that from a perfect crystalline 6H–SiC.

3.4. Micro-photoluminescence under 325 nm UV excitation

Fig. 5 exhibits RT Micro-photoluminescence (μ-PL) spectra of several hot and RT C^+–Al^+co-implanted 6H–SiC. The non-implanted corner shows a strong RT PL band at 2.93 eV, due to the free-to-bound transition involving nitrogen, FB_N, with a 100 meV phonon side band in its low energy side [21]. A deeper and very broad band with the peak energy at ~2.1 eV might be due to the defects related emissions and its origin is unknown yet. After the C^+–Al^+ co-implantation, these PL emissions, in particular the FB_N band, are weakened considerably, as shown in Fig. 5(b) and (d) for two un-annealed C–Al co-implanted samples, indicating the severe damage of the crystalline structure. However, the PL spectrum in Fig. 5(b) for a hot (600 °C) implanted sample E5 still showed the FB_N band and the 2.1 eV band although they are very weak, while the spectrum in Fig. 5(d) for a RT implanted one showed no features at 2.1 eV and only a very broad bump between 2.5–3.4 eV. This

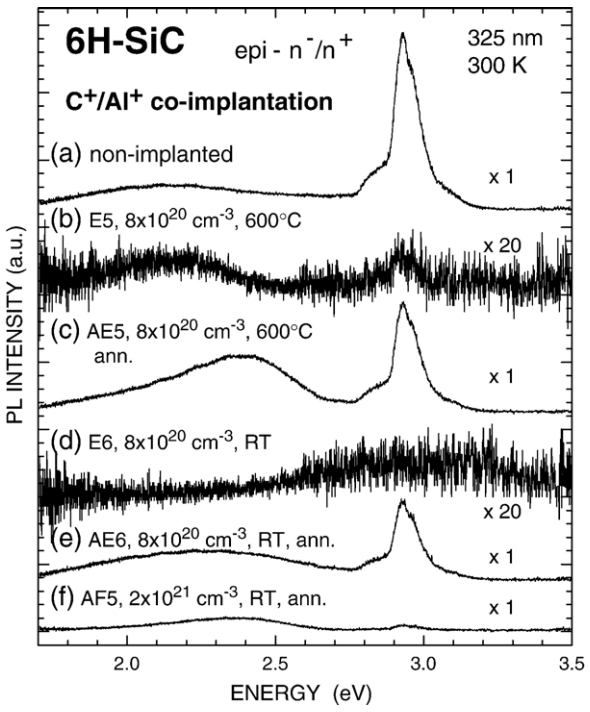

Fig. 5. RT μ-PL probing from n^-/n^+epitaxial 6H–SiC: (a) non-implanted, (b) non-annealed (E5) and (c) annealed (1,550 °C) (from E5, AE5) Al^+–C^+ hot (600 °C) co-implanted with C–Al concentration of 8×10^{20} cm^{-3}, (d) non-annealed (E6) and (e) annealed (from E6, AE6) RT Al^+–C^+ co-implanted with C–Al doses of 8×10^{20} cm^{-3}, and (f) annealed (AF6) RT Al^+–C^+ co-implanted with C–Al doses of 2×10^{21} cm^{-3}.

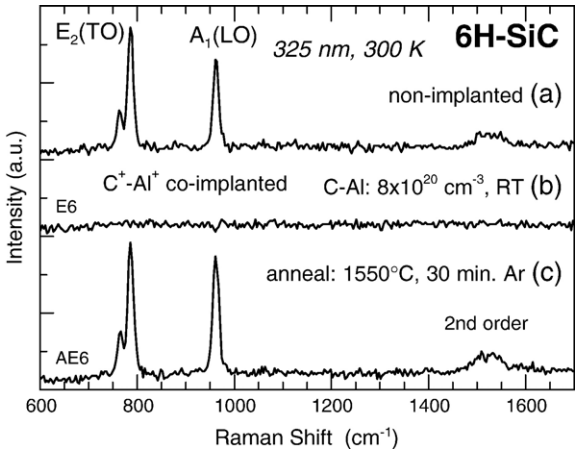

Fig. 6. Raman spectra from a n^-/n^+ epitaxial 6 H–SiC, E-6 (RT Al^+–C^+: 8×10^{20} cm^{-3}), excited under 325 nm, for (a) non-implanted corner, and Al^+–C^+ co-implanted region (b) before and (c) after annealing.

comparison indicates that the hot implanted sample has less damage than the RT implanted one.

Through annealing at 1550 °C for 30 min on above mentioned implanted samples in Figs. (b) and (d), the FB_N band was re-covered with its peak intensity close to the value before implantation in both cases, as shown in Fig. 5(c) and 5 (e). For the hot-implanted/annealed sample, a new broad PL band with the peak energy at ~2.4 eV appeared, as shown in Fig. 5(c), superimposed on the defects-related 2.1 eV band. This is from the Al acceptor [21] or C–Al complex. However, for the RT implanted/annealed sample with the same amount of implanted doses (C^+/Al^+: 8×10^{20} cm^{-3}) and after annealing under the same conditions, there exists a very broad band spreading over 1.7–2.7 eV. It is most likely due to a combination of the deep defect 2.1 eV band and the Al-activated 2.4 eV band. This means that the RT implanted/annealed sample after annealing produced weaker or less amount Al-acceptor activation than the hot-implanted sample.

Furthermore, Fig. 5(f) exhibits a PL spectrum from a sample with the highest RT implanted doses (C^+/Al^+: 2×10^{21} cm^{-3}), much higher than the one in Fig. 5(e), and after annealing. The FB_N band in Fig. 5 (f) is much weaker than that in Fig. 5(e), and its Al-acceptor activated 2.4 eV band component is weaker than one in Fig. 5(e) also. This indicates that too high an implantation dose will make it difficult to anneal out implantation damage completely.

3.5. Raman scattering under UV 325 nm excitation

To better understand the spectral behavior from these co-implanted samples, further Raman measurements using other excitation wavelengths, such as 488 nm and 325 nm, were performed. When the 488 nm excitation was applied, the RT implanted samples showed Raman spectra with three Si–Si, Si–C and C–C amorphous bands similar to that of Fig. 3(a)–(c), but without the superposed sharp crystalline 6H–SiC features of E_2 (TO) and A_1(LO) (not shown here). This indicates that the 488 nm laser line can probe the implantation induced amorphous SiC layer but can not penetrate through it to probe the underneath crystalline 6H–SiC.

Fig. 6 shows the UV (325 nm) excited μ-RS probe on a n^-/n^+ epitaxial 6H–SiC, E3, with RT implantation doses of 2×10^{21} cm^{-3} for both $C^+$and Al^+. From the non-implanted corner, 6H–SiC characteristic E_2(TO) and A_2(LO) modes are exhibited. After C^+–Al^+ RT co-implantation, neither these Raman features nor the broad amorphous bands can be detected under the same measurement conditions, unlike the case of 514 nm excitation as shown in Fig. 3(a)–(c). However, after high temperature annealing, the crystalline 6H–SiC characteristic Raman E_2(TO) and A_2(LO) features are re-covered as shown in Fig. 6(c). Because the laser probe depth of the 325 nm excitation is much less than that of the 514 and 488 nm excitations, this shows that the near surface 6H–SiC layers were badly damaged under RT C^+–Al^+ co-implantation, however, after high-T annealing, the implanted layers are recovered with good crystallinity.

The dramatic changes in above micro-probing RS-PL spectra for 6H–SiC can be explained from the behavior of the absorption coefficient of the implantation induced a-SiC layer [16]. The above results show that the 514 nm light can penetrate through the 0.2 μ amorphous SiC layer slightly, the 488 nm light can not, and the 325 nm light can probe the very top thin layer of SiC only.

Further temperature-dependent studies of μ-RS were also performed (data not shown here). The major A_1(LO) and E_2 (TO) 6H–SiC modes can be detected from all the C^+–Al^+ co-implanted/annealed samples over a wide range of temperature, 80–870 K and they are very close to the spectra from non-implanted 6H–SiC. These provide a further evidence of the recrystallization of the C–Al co-implanted/annealed 6H–SiC and the activation of implant acceptors. Further analyses will provide more supports on our conclusions in details.

3.6. Fourier transform infrared (FTIR) reflectance

Fig. 7 shows FTIR reflectance spectra of an Al–C co-implanted (both with 6×10^{20} cm^{-3} at RT) 6H–SiC, E-3, before and after annealing. The reststrahlen band between 750–1000 cm^{-1} is

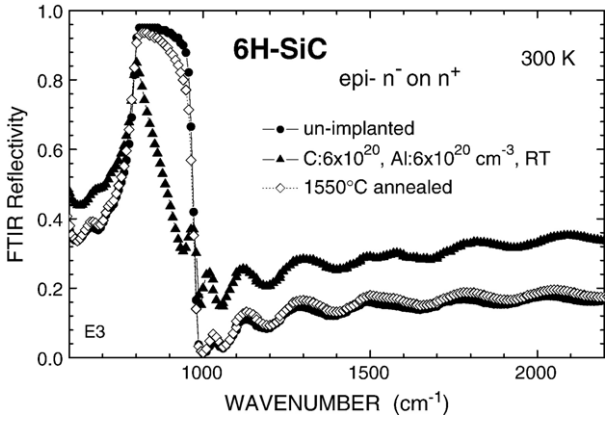

Fig. 7. FTIR reflectance of a 6 H–SiC co-implanted with C and Al ions at 20×10^{20} cm^{-3}, before and after annealing.

characteristic of 6H–SiC with the low frequency rising edge close to the 6H–SiC transverse optical (TO) phonon frequency and the dip beyond the high frequency falling edge close to the longitudinal optical (LO) phonon frequency. It was reported [22] that the reflectance at the top of the reststrahlen band is sensitive to the surface condition of the SiC material/film and that a rough surface could cause the reflectance to drop from the low frequency edge to the high frequency edge. We have performed a theoretical calculation on the infrared (IR) reflectance spectra of 6H–SiC based upon the effective medium model [23]. It was indicated that the amorphization of the implanted layer is responsible for the presence of the deep reflection dip at $\sim 930\ cm^{-1}$, which is exactly seen from Fig. 7. The FTIR spectral shape in Fig. 7 reflects the severe damage of 6H–SiC due to the ion implantation and good structural recovery from annealing.

4. Conclusion

In summary, a series of hot (600 °C) and RT aluminum–carbon ion co-implanted 6H–SiC epitaxial films and effects of high temperature (HT), 1550 °C, annealing were studied by the combination of structural and optical analytical techniques. Al–C ion implantation caused the damage of 6H–SiC, which were revealed with multiple X-ray diffraction (XRD) patterns, the decrease and decline of the top shape of the FTIR reflectance phonon band, the minimization of the 6H–SiC characteristic 2.9-eV band edge photoluminescence (PL) emission, and the appearance of amorphous SiC related broad Raman bands. The high temperature annealing induces an out-diffusion and re-distribution of implanted Al evidenced by secondary ion mass spectroscopy, smoothens and narrows the XRD patterns, recovers the 6H–SiC characteristic FTIR band shape, refreshed the 6H–SiC band edge PL emission band, decreases and eliminates the amorphous SiC Raman features. These indicate the recovery of the crystallinity of 6H–SiC from the high temperature annealing over the Al–C ion implantation. Raman micro-probing also indicated that the hot co-implantation causes less damage on the SiC crystal that the RT implantation. UV PL RT micro probing further confirmed the activation of the p-type dopants from Al acceptors after HT annealing, and revealed this activation superior in hot implanted sample than the RT implanted one. Too high dose level of co-implantation beyond $2\times10^{21}\ cm^{-3}$ led to a poor activation of Al acceptors. Our results have shown that C–Al co-implantation, under proper implantation and annealing conditions, is a good way to realize good p-type doping in SiC materials.

Acknowledgment

This work was supported from funds at National Taiwan University by the National Science Council (NSC) 94-2215-E-002-019 and 95-2221-E-002-118, and at Fisk University by the NSF (Grant No: HRD-0420516) Center for Physics and Chemistry of Materials.

References

[1] W.J. Choyke, H. Matsunami, G. Pensl (Eds.), Silicon Carbide: Recent Major Advances, Springer, Berlin, 2004.
[2] Z.C. Feng, J.H. Zhao ed., Silicon Carbide: Materials, Processings and Devices, Vol. 20 in a book series, Optoelectronic Properties of Semiconductors and Superlattices, Chief ed. M. O. Manasreh, Taylor & Francis Books, Inc., New York, 2003.
[3] Z.C. Feng (Ed.), SiC Power Materials — Devices and Applications, Springer, Berlin, 2004.
[4] A.A. Lebedev, Semicond. Sci. Technol. 21 (2006) R17.
[5] Z.C. Feng, Microelectron. Eng. 83 (2006) 165.
[6] R.F. Davis, G. Kelner, M. Shur, J.W. Palmour, J.A. Edmond, Proc. IEEE 79 (1991) 677.
[7] G.L. Harris, in: G.L. Harris (Ed.), Properties of Silicon Carbide, Short Run Press, Exeter, UK, 1995.
[8] M.V. Rao, P. Griffiths, O.W. Holland, G. Kelner, J.A. Freitas Jr., D.S. Simons, P.H. Chi, M. Ghezo, J. Appl. Phys. 77 (1995) 2479.
[9] Y. Hirano, T. Inada, J. Appl. Phys. 77 (1995) 1020.
[10] L. Calcagno, M.G. Crimaldi, P. Musumeci, J. Mater. Res. 12 (1997) 1727.
[11] T. Kimoto, N. Inoue, H. Matsunami, in: W.J. Choyke, H. Matsunami, G. Pensl (Eds.), Fundamental Questions and Applications of SiC (Part II), special issue, Phys. Stat. Sol. (a), vol. 161, 1997, p. 263.
[12] M.V. Rao, P. Griffiths, J. Gardner, O.W. Holland, M. Ghezzo, J. Hretchmer, G. Kelner, J.A. Freitas, J. Electron. Mater. 25 (1996) 75.
[13] T. Troffer, M. Schadt, T. Frank, H. Itoh, G. Pensl, J. Heidl, H.P. Strunk, M. Maier, in [3], p.277.
[14] J.H. Zhao, K. Tone, S.R. Weiner, M.A. Caleca, H. Du, S.P. Withrow, IEEE Electron Device Lett. 18 (1997) 375.
[15] K. Tone, J.H. Zhao, IEEE Trans. Electron Devices 46 (1999) 612.
[16] Z.C. Feng, S.J. Chua, K. Tone, J.H. Zhao, Appl. Phys. Lett. 75 (1999) 472.
[17] S.M. Sze, VLSI Technology, McGraw Hill, New York, 1988, Chapter 8.
[18] J.W. Mayer, S.S. Lau, Electronic Materials Science, Macmillan, New York, 1990, Chapter 8.
[19] V.N. Makarov, D.A. Plotkin, A.V. Suvorov, Inst. Phys. Conf. Ser. 137 (1994) 545.
[20] D.W. Feldman, J.H. Parker Jr., W.J. Choyke, L. Patrick, Phys. Rev. 170 (1968) 698.
[21] M. Yoganathan, W.J. Choyke, R.P. Devaty, P.G. Neudeck, J. Appl. Phys. 80 (1996) 1763.
[22] R.T. Holm, P.H. Klein, P.E.R. Nordquist Jr., J. Appl. Phys. 60 (1986) 1479.
[23] W. Chang, Z.C. Feng, J. Lin, R. Liu, A.T.S. Wee, K. Tone, J.H. Zhao, Surf. Interface Anal. 33 (2002) 500.